Synthesis and Characterization of Hydroxyapatite/Alginate Composites: Study of pH and Sintering Influenced on the Structural, Morphological, and Clindamycin Release Behavior

Wulandari Wulandari, Dini Muthi'ah Islami, Novesar Jamarun*, Diana Vanda Wellia, and Emriadi Emriadi

Department of Chemistry, Faculty of Mathematics and Natural Sciences, Universitas Andalas, Limau Manis, Padang 25163, Indonesia

* **Corresponding author:**

email: novesarjamarun@sci.unand.ac.id

Received: May 18, 2023
Accepted: January 3, 2024

DOI: 10.22146/ijc.84558

Abstract: *The hydroxyapatite/alginate (HAp/Alg) composite was synthesized using an* in-situ *precipitation route. The effect of pH (8, 9, 10, and 11) and calcination temperature (300, 500, 700, and 900 °C) were studied by characterization techniques such as X-ray diffraction (XRD), Fourier-transform infrared (FTIR), and scanning electron microscopy with energy-dispersive X-ray (SEM with EDAX). XRD results show the hexagonal crystal system of HAp for each pH value and the biphase (HAp and whitelockite) for the sintering temperature at 700 and 900 °C. The FTIR spectra show no impurity peaks. SEM images revealed spherical-like (HAp/Alg-11) and flake-like (HAp/Alg-900) particles with good homogeneity, size, and shape that could be notable for biomedical utilization, such as drug delivery material. Drug loading and release ability of pure HAp, HAp/Alg-11, and HAp/Alg-900 composites have been investigated with clindamycin hydrochloride as the drug model. The maximum clindamycin HCl release from HAp, HAP/Alg-11, and HAp/Alg-900 reached 74.48, 92.75, and 69.65% in the 8th hour. HAp/Alg-11 has the highest release because it has the largest surface area of 162.584 m^2/g. Antibacterial test results showed HAp/Alg-11 has antibacterial activity against* Staphylococcus aureus *and* Escherichia coli*, confirming that HAp/Alg-11 composite has the potential to be applied as drug delivery.*

Keywords: *alginate; clindamycin hydrochloride; composite; drug release, hydroxyapatite*

■ INTRODUCTION

In recent years, calcium phosphate materials have become an interesting research topic for scientists because of their wide applications in the health and medicinal fields [1-3]. Hydroxyapatite (HAp), $Ca_{10}(PO_4)_6(OH)_2$ [4], one of the calcium phosphate materials, has excellent biocompatibility, bioactivity, and osteoconductivity properties due to the similar traits that it has to the main constituent components of human bones and teeth [5-7]. HAp can be synthesized from synthetic and natural sources. The use of natural sources will be preferred because it reduces the use of harmful chemicals and is more economical and environmentally friendly [8]. This study used a natural source, such as bamboo shell waste, because it contains high calcium [9]. The HAp synthesis methods include precipitation, hydrothermal, solid state, microemulsion, and sol-gel [10]. In this study, the precipitation method will be used because of several things such as simple, low cost, takes a short time, and the product has good properties [1].

To get more advantages of HAp, many scientists combine HAp with other materials, such as polymer [11-14], to obtain composite material. Sanchez et al. [15] have successfully synthesized nanocomposite films of chitosan-HAp-MWCNT. These films contain 5.0% weight of HAp nanoparticles and 0.5% weight of MWCNT. The films demonstrate exceptional tensile characteristics and conductivity. Madhumathi et al. [12], also reported the synthesis of β-chitin–HAp composite, whereas apatite on the β-chitin membrane surfaces

increased cell attachment and dispersing. The β-chitin-HAp composite membranes, subjected to 3 and 5 cycles of immersion, exhibited enhanced cell adhesion and higher cell count. This approach enhanced the biocompatibility of β-chitin membranes by promoting the deposition of the apatite layer. These membranes are suitable for tissue engineering applications [12].

Our topic research focused on the HAp/Alg composite synthesis and studied synthesis parameters such as concentration, pH, and sintering temperature. Previous research reported the synthesis of HAp/Alg composite with alginate concentrations 9.1, 16.7, 23.1, 28.6, and 33.3 w/w% [9]. SEM results showed HA 33.3% has a smaller particle size and uniform shape. In addition, the TGA-DTA result revealed that the thermal resistance of HAp/Alg composite was increased due to alginate attendance so that it could be utilized in several sophisticated applications, such as bioimaging and medication delivery [9].

This research investigates the impact of sintering temperature on the structural and morphological characteristics using analytical methods, including X-ray diffraction (XRD), Fourier-transform infrared (FTIR) spectroscopy, and scanning electron microscopy combined with energy-dispersive X-ray (SEM-EDX) spectroscopy. Alginate, a polymer with many crosslinks, can increase the degree of swelling and can control the drug-release process [16-17]. The drug release capacity was studied by using clindamycin HCl as a drug model because it is an antibiotic to treat osteomyelitis caused by bacterial infections such as *S. aureus* and *E. coli*. The antibacterial assay also was investigated through a diffusion method to compare the antibacterial activities before and after clindamycin HCl loading into the composite. This study aims to determine the potential or opportunity for HAp/Alg composites to be developed as drug delivery materials, especially clindamycin HCl.

■ EXPERIMENTAL SECTION

Materials

Bamboo shell, *Sollen* spp. waste was obtained from a seafood restaurant in Padang, West Sumatra, Indonesia. The analytical grade of ammonia solution 25% (NH_4OH), diammonium hydrogen phosphate ($(NH_4)_2HPO_4$), nitric acid (HNO_3), dimethyl sulfoxide (DMSO), nutrient agar (NA), and Mueller Hinton agar (MHA) were purchased from Merck, Darmstadt, Germany. Alginate impression materials were obtained from Shanghai Medical Instrument, Shanghai, China. Clindamycin HCl as a drug model for drug delivery assay was obtained from PT. Etercon Pharma, Indonesia.

Instrumentation

XRD analysis was carried out by PAN analytical using Cu-Kα radiation (1.54 Å) with 0.02° step size. The FTIR spectrum was studied using PerkinElmer Version 10.6.1. The morphological analysis of the powder samples was examined using electron microscopy SEM Thermoscienticic Quatro S assisted by an EDX spectroscope (EDS Ametek EDAX), operated at 15 Kv. The Brunauer, Emmett, and Teller (BET) and Barrett-Joyner-Halenda (BJH) investigations are performed to investigate the physical characteristics of materials, including pore size and volume, BET surface area, and adsorption-desorption isotherms.

Procedure

Synthesis of HAp/Alg composite

Based on our previous study [9], calcium oxide was synthesized using bamboo shell wastes. Calcium oxide and $(NH_4)_2HPO_4$ powder with a Ca/P molar ratio of 1.67 were dissolved in 50 mL of HNO_3 and aquadest. A $(NH_4)_2HPO_4$ solution at 80 °C for 2 h (the alginate 33.3 w/w% was the optimum concentration based on our previous study [9]. This solution was then dropwise added to the calcium oxide solution and continuously stirred for 2 h while adjusting the pH of 8, 9, 10, and 11. The sample was labeled HAp/Alg-8, HAp/Alg-9, HAp/Alg-10 and HAp/Alg-11. The obtained precipitate was filtered with Whatman No.41 filter paper and was rinsed until the pH was 7. The resulting solid was dried at 120 °C for 5 h to obtain the HAp/Alg composite. The HAp/Alg-11 as optimum composite was sintered at 300, 500, 700, and 900 °C. Then, the sample was labeled HAp/Alg-300, HAp/Alg-500, HAp/Alg-700, and HAp/Alg-900. The procedure flowchart is shown in Fig. 1.

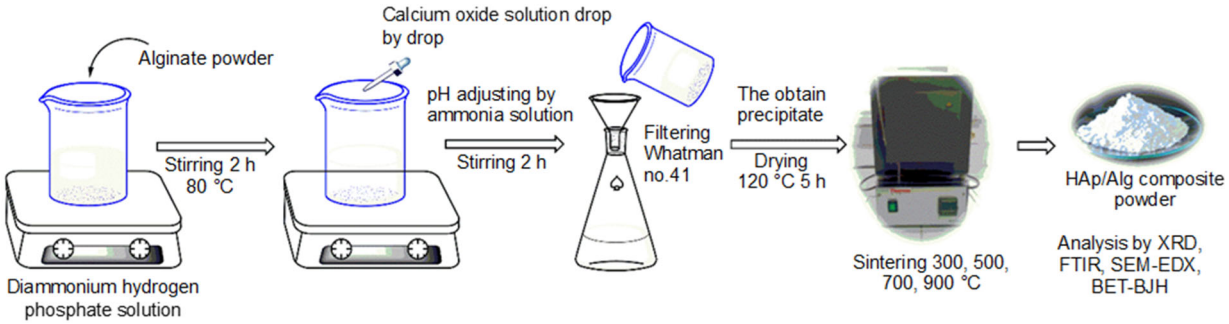

Fig 1. The procedure flowchart of the research

Drug release test

A solution was made by diluting 3 mg of clindamycin HCl in 50 mL of distilled water. The mixture underwent a 2 h stirring period at ambient temperature. Afterward, 10 mg of the sample powder was added to the solution and stirred for 24 h at a temperature of 37 °C. Following centrifugation, the mixture was desiccated at ambient temperature for 7 d. The clindamycin loaded-HAp and HAp/Alg composite samples were dissolved in 50 mL of phosphate-buffered saline (PBS) with a pH of 7.3. They were then placed on a magnetic stirrer at a speed of 100 rpm and maintained at a temperature of 37 °C. A volume of 5 mL was obtained from the samples at intervals of 0, 1, 2, 3, 4, 5, and 6 h. To maintain a consistent sample volume of 50 mL, an extra 5 mL of PBS was added. The samples were examined using a UV-vis spectrophotometer configured to function at a specific wavelength of 210 nm [18]. The sample's overall drug release capacity was quantified as a percentage (t%).

Antibacterial assay

The antibacterial activity of HAp and HAp/Alg composite against *E. coli* and *S. aureus* bacteria was evaluated using the diffusion method [19]. Initially, 1 mL of the DMSO solvent was employed to thoroughly dissolve 10 mg of the materials. Subsequently, bacterial isolates obtained from NA media plates were transferred to a fresh NA medium by gently scratching them with a sterile ose needle in a zigzag pattern. Subsequently, the NA medium was incubated with the bacteria for 24 h. Next, the MHA medium was inoculated with the bacteria using the streaking technique. Then, a pipette transferred 30 µL of the HAp, HAp/Alg-11, and HAp/Alg-900 samples into agar wells measuring 7 mm in diameter. The petri dish was incubated aerobically at 37 °C for 24 h. The size of the zone of inhibition was assessed after 24 h of incubation. Clindamycin HCl and DMSO were used as the positive and negative controls, respectively.

■ RESULTS AND DISCUSSION

Effect of pH on Crystallinity and Morphology of HAp/Alg Composites

Crystals structure analysis

The XRD patterns of HAp, Alg, and HAp/Alg composite with various pH values at 2θ = 15–55° are shown in Fig. 2(a-f). All diffraction peaks in the XRD patterns of HAp and HAp/Alg composite in Fig. 2(a, c, d, e, f) at 2θ = 25.96°, 31.86°, 32.16°, 32.46°, 34.08°, 39.86°, 46.78°, 49.48°, 53.28° are well-matched with the

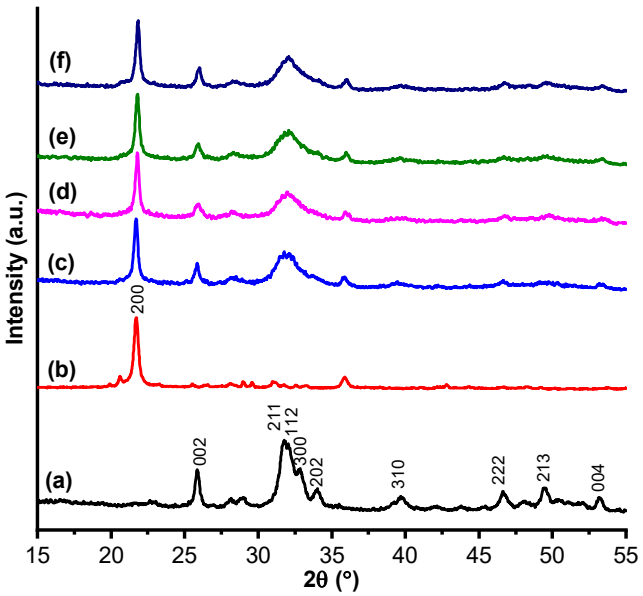

Fig 2. XRD patterns of (a) HAp, (b) Alg, (c) Hap/Alg-8, (d) Hap/Alg-9, (e) HAp/Alg-10, and (f) HAp/Alg-11

Table 1. The crystallite size of HAp in HAp/Alg composites with different pH values

Sample	Crystallite size (nm)
HAp	21.78
HAp/Alg-8	24.04
HAp/Alg-9	21.62
HAp/Alg-10	21.25
HAp/Alg-11	30.45

hexagonal phase of HAp (ICSD #157481) with P 63/m space group [7,11,13,20-21]. It shows that all the synthesized samples with various pH values are well crystallized. However, there are differences in the intensity of the diffraction peaks of HAp/Alg compared to pure HAp. It happened due to the influence of adding Alg to form the composite, proven by the distinctive peak at 21.71° having (200) crystal plane [22].

Based on the intensity of each diffraction pattern, the below shows that the difference in pH has an insignificant effect on the crystallinity of the composite. However, pH impacts the change of crystallite size of HAp in the HAp/Alg composite, as shown in Table 1. The Debye-Scherrer equation (Eq. (1)) can be used to calculate the average crystal size.

$$D = \frac{k\lambda}{\beta \cos\theta} \quad (1)$$

The variables in the equation are defined as follows: λ represents the wavelength of the Cu-Kα radiation (1.5406 Å), K represents the Scherrer constant (0.89), β represents the full-width radiants at half maximum (FWHM) of the diffraction line, and θ represents the Bragg diffraction angle [23]. The crystallite size of HAp, HAp/Alg-8, HAp/Alg-9, HAp/Alg-10, and HAp/Alg-11 is 21.78, 24.04, 21.62, 21.25, and 30.45 nm, respectively. The concentration of specific ions in solution can change significantly at very high pH. These changes can affect the saturation of the solution and the conditions that favor the growth of larger crystals. At pH 11, these conditions may be more favorable for more considerable crystal growth than at other pHs.

FTIR analysis

The FTIR spectrum of the HAp-Alg composite with various pH values at wavenumbers 4000–400 cm^{-1} is shown in Fig. 3(a-d). Absorption bands were observed at 472, 563, 603, and 1035 cm^{-1} for the PO_4^{3-} group [24-26]. The deep and wide band at 3435 cm^{-1} is associated with the composite's vibrations of O–H stretching [27-28]. The detected absorption band at 792 cm^{-1} stands for the C–H of Alg. Alongside that, two carboxylic group bands were detected at 1637 and 1421 cm^{-1}, representing the prominent characteristic bands of the Alg [16,24]. The FTIR results corroborate the XRD results, where it is proven that HAp/Alg composites are formed at all pH variations, and there are no traces of impurities made during the reaction took place. The difference in pH impacts shifting the absorption band, compared with OH stretching of pure HAp at 3359 cm^{-1} in the previous report [9], as shown in detail in Table 2. The O–H vibrational absorption band at wavenumber 3359 cm^{-1} has shifted towards lower wavenumbers, indicating lower energy and the formation of more robust interactions between HAp and alginate in the formation of HAp/Alg composites.

SEM-EDX analysis

The morphological characteristics and elemental composition of the HAp/Alg powders were picturized and analyzed using SEM-EDX. Fig. 4 shows the SEM images and particle size histograms of HAp/Alg-8 (a&e), HAp/Alg-9 (b&f), HAp/Alg-10 (c&g), and HAp/Alg-11 (d&h).

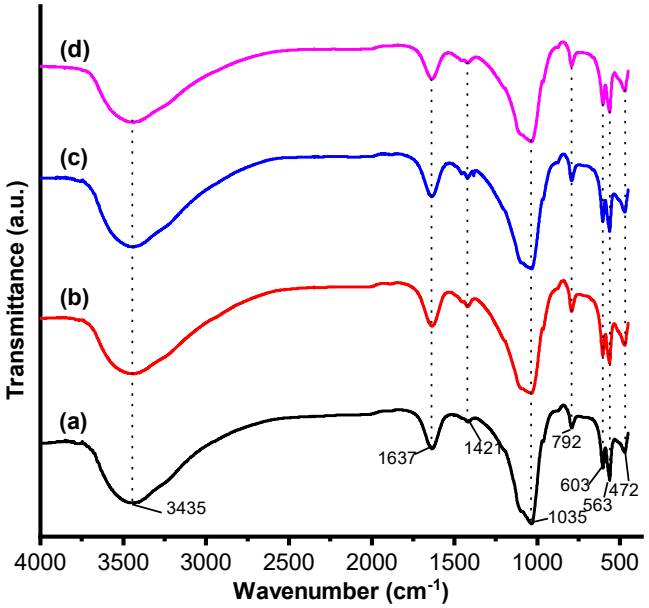

Fig 3. FTIR spectra of (a) HAp, (b) Alg, (c) HAp/Alg-8, (d) HAp/Alg-9, (e) HAp/Alg-10, and (f) HAp/Alg-11

Table 2. Functional group of HAp/Alg composites with different pH values

	Wavenumber (cm^{-1})			
	HAp/Alg-8	HAp/Alg-9	HAp/Alg-10	HAp/Alg-11
Phosphate (PO_4^{3-})				
ν_2 bending	472.05	471.57	471.78	471.80
ν_3 asymmetric stretching	1035.42	1036.94	1035.74	1035.95
ν_4 bending	563.44, 603.32	563.92, 604.14	563.68, 604.56	563.58, 603.29
COO asymmetric stretching	1637.53	1633.95	1637.55	1639.08
COO symmetric stretching	1420.889	1422.93	1421.20	1421.96
C–H of Alg	792.59	792.71	792.52	792.66
O–H stretching	3435.59	3435.88	3435.88	3435.81

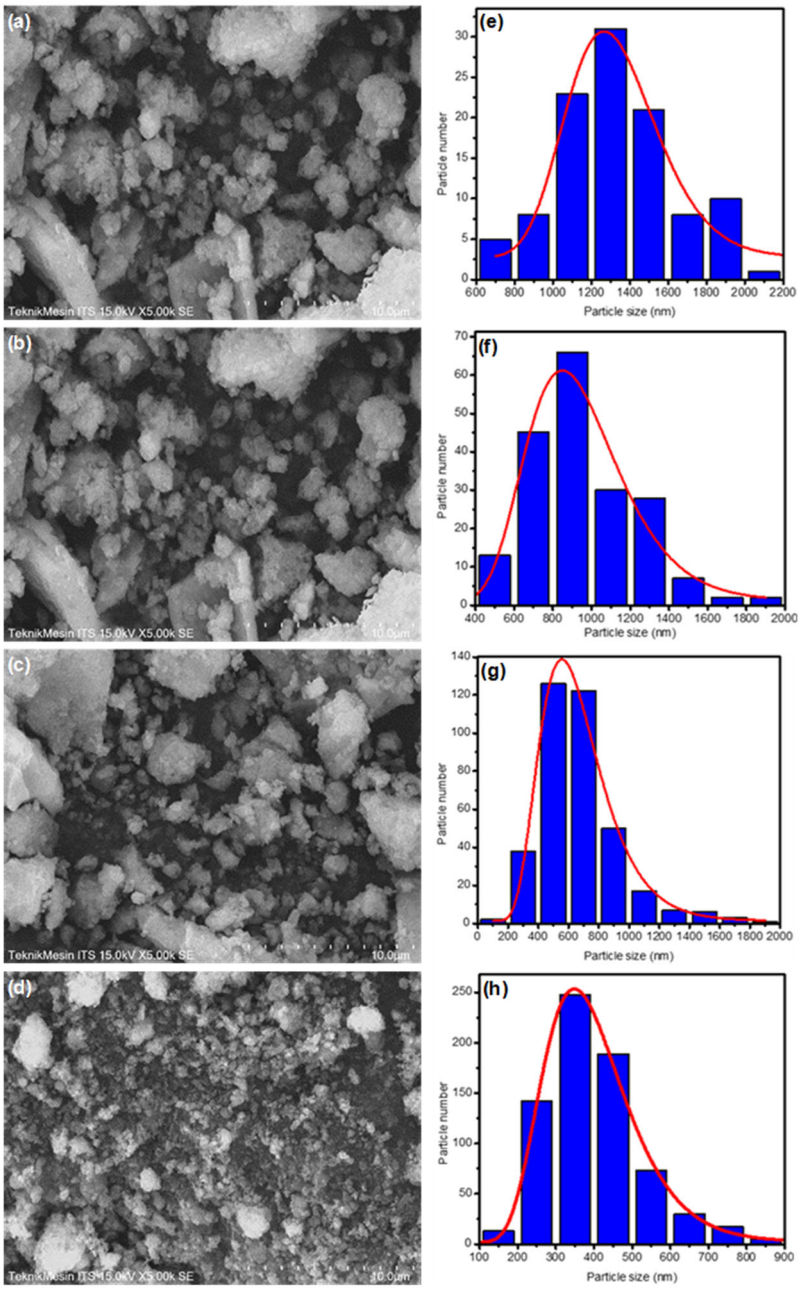

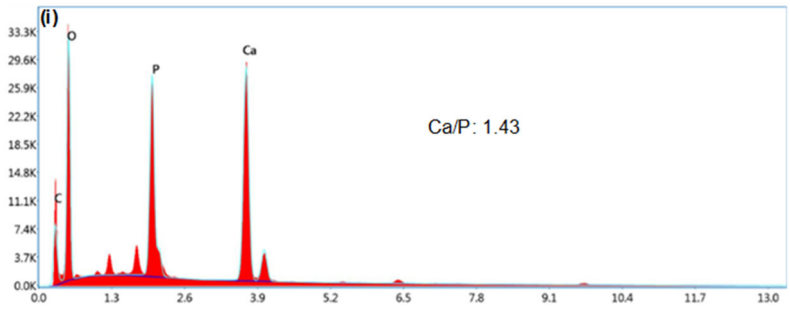

Fig 4. SEM images and particle size histogram of (a&e) HAp/Alg-8, (b&f) HAp/Alg-9, (c&g) HAp/Alg-10, (d&h) HAp/Alg-11, and (i) EDAX of HAp/Alg composite

Table 3. The average particle size of HAp/Alg composites with different pH values

Sample	Average particle size (nm)
HAp/Alg-8	1362
HAp/Alg-9	958
HAp/Alg-10	669
HAp/Alg-11	401

The morphology of HAp/Alg at various pH levels tends to be irregularly spherical and agglomerated. At alkaline conditions, the mobility rate of Ca^{2+} and PO_4^{3-} ions is fast due to the high kinetic energy, so they collide quickly, leading to some agglomeration [29]. The average particle size at each pH value is different, as shown in Table 3. The average particle size is 1362, 958, 669, and 401 nm for the HAp/Alg-8, HAp/Alg-9, HAp/Alg-10, and HAp/Alg-11, respectively. In conclusion, as the pH value rises, the average particle size tends to be more petite and uniform, although some agglomeration exists [30].

Next, the EDX spectrum exhibited the peak of Ca, P, C, and O elements of the HAp/Alg composite that graphed in Fig. 4(i). The molar ratio of Ca/P was obtained at 1.43 (lower than 1.67), caused by the presence of carbon from Alg. The appearance of the carbon element proves that there is an interaction between Alg and HAp to form HAp/Alg composite. The setting of pH values during the reaction affected the morphology of the composite. Fig. 4 displayed that the obtained particle size of HAp/Alg-11 is smaller than others, and the particle shape tends to be uniform compared to other composites. So, HAp/Alg-11 was chosen as the optimum sample and continued with sintering at various temperatures.

The Effect of Calcination Temperature on Crystallinity and Morphology of HAp/Alg Composites

XRD analysis

The diffraction patterns of the HAp/Alg composite in different sintering temperatures at 2θ = 15–55° are shown in Fig. 5(a-e). The pure hexagonal phase was obtained for HAp/Alg-300 and HAp/Alg-500, and no new phase appeared. However, HAp/Alg-700 and HAp/Alg-900 have a new phase, such as whitelockite. It agrees with research conducted by Jarudilokkul et al. [31], who reported that the crystallization of HAp occurs at 635 °C, and the other phases of calcium phosphate, such as TCP and whitlockite, appeared as passing through

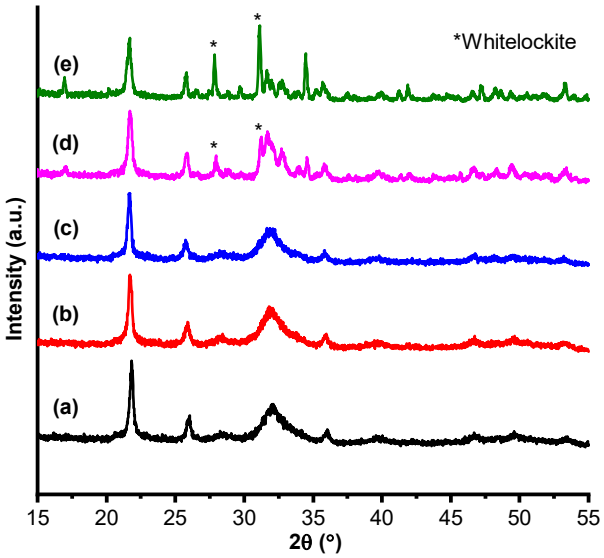

Fig 5. XRD patterns of HA composite at (a) HAp/Alg, (b) HAp/Alg-300 (c) HAp/Alg-500, (d) HAp/Alg-700, and (e) HAp/Alg-900

that temperature [31]. Chen et al. [32], also reported that the increasing sintering temperature caused HAp to lose the –OH group, changing its structure to another phase [32]. The phase transformation from HAp to whitelockite may also impact the growth of larger crystals. The phase change may trigger more significant crystal growth in whitelockite, resulting in larger crystal sizes than HAp in HAp/Alg composite, as shown in Table 4.

FTIR analysis

The FTIR spectrum of the HAp-Alg composite with various sintering temperatures at wavenumbers 4000–400 cm^{-1} is shown in Fig. 6(a-e). The absorption bands appear at the exact wavenumber as the FTIR spectrum of pH value variation in Fig. 3. However, the rising sintering temperature decreases the OH stretching intensity mode at 3435 cm^{-1}. It indicates that water content decreases to form the stable HAp/Alg composite [30]. Chen et al. [32], also stated that hydroxyapatite could lose –OH group when the sintering temperature was increased, and the structure will transform to form another phase, such as whitelockite, $Ca_9(PO_4)_6PO_3OH$. The difference in sintering temperature impacts on shifting the absorption band, compared with OH stretching of pure HAp at 3359 cm^{-1} in the previous report [9], as shown in detail in Table 5.

SEM-EDX analysis

SEM images show that the calcination temperature plays a vital role in determining the morphology of a material. Fig. 7 displays the SEM pictures of the HAp/Alg composites powder with different sintering temperatures for HAp/Alg-300 (a), HAp/Alg-500 (b), HAp/Alg-700 (c), and HAp/Alg-900 (d). As the sintering temperature increased to 900 °C, the morphology changed and formed a uniform flake-like particle shape. HAp/Alg-900

Table 4. Average crystallite size of HAp in HAp/Alg composites with different sintering temperatures

Sample	Crystallite size (nm)
HAp/Alg	30.45
HAp/Alg-300	22.05
HAp/Alg-500	20.54
HAp/Alg-700	38.30
HAp/Alg-900	48.97

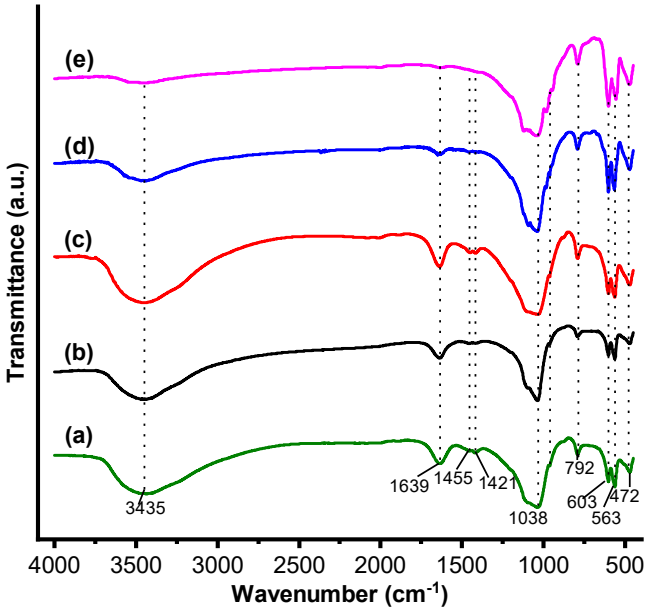

Fig 6. FTIR spectra of HAp/Alg composite of (a) HAp/Alg, (b) HAp/Alg-300 (c) HAp/Alg-500, (d) HAp/Alg-700, and (e) HAp/Alg-900

Table 5. The functional group of HAp/Alg composites with different sintering temperatures

	Wavenumber (cm^{-1})				
	HAp/Alg	HAp/Alg-300	HAp/Alg-500	HAp/Alg-700	HAp/Alg-900
Phosphate (PO_4^{3-})					
ν_2 bending	471.80	472.40	471.60	472.75	472.62
ν_1 symmetric stretching	-	-	964.15	963.81	-
ν_3 asymmetric stretching	1035.95	1038.91	1039.68	1039.33	1038.62
ν_4 bending	563.58, 603.29	563.94, 603.26	564.61, 603.29	567.17, 603.33	557.55, 603.00
COO asymmetric stretching	1639.08	1639.58	1637.94	1650.80	1634.83
COO symmetric stretching	1421.96	1455.17	1450.50	-	-
C–H of alginate	792.66	792.34	792.47	792.96	792.94
O–H stretching	3435.81	3435.78	3435.78	3435.72	3435.57

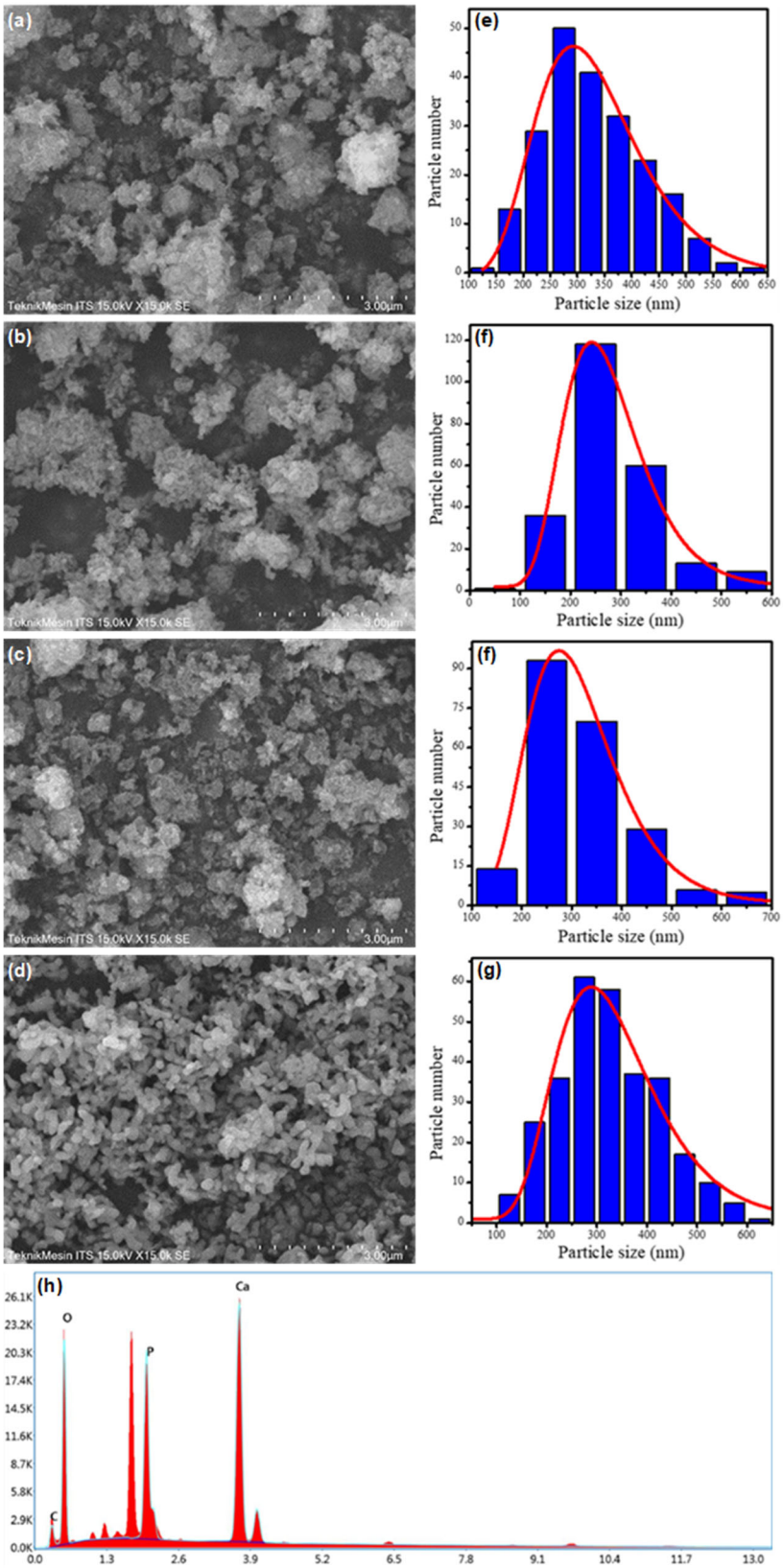

Fig 7. Morphology depiction of HAp/Alg composite, (a & e) HAp/Alg-300, (b & f) HAp/Alg-500, (c & g) HAp/Alg-700, (d & h) HAp/Alg-900, and (i) EDAX of HAp/Alg-900

Table 6. The average particle size of HAp/Alg composites with different sintering temperatures

Sample	Average particle size (nm)
HAp/Alg-300	332.65
HAp/Alg-500	294.69
HAp/Alg-700	323.26
HAp/Alg-900	323.78

has good homogeneity, size, and shape that could attend as a notable aspiring for biomedical utilization such as drug delivery material. Fig. 7(e-h) shows the histogram of the particle size of each sintering temperature variation. The average particle size is 332.65, 294.69, 323.26, and 323.78 nm for HAp/Alg-300, HAp/Alg-500, HAp/Alg-700, and HAp/Alg-900, respectively, as shown in Table 6. It can be seen that the average particle size of HAp/Alg-700 and HAp/Alg-900 increases from 323.26 to 323.78 nm. It occurs due to the evaporation of the residue and diffusion between grain boundaries of the particles, causing the formation of interconnected flake-like particles [30].

The illustrated EDAX spectrum (Fig. 7(i)) showed each of the elements that contributed to the formation of the HAp/Alg composite. From EDAX the calculated Ca/P molar ratio was found to be 1.69. The presence of the C element marked the interaction of alginate and hydroxyapatite in the composite formation.

BET-BJH analysis

The surface areas of the pure HAp, HAp/Alg-11, and HAp/Alg-900 samples were examined using the BET nitrogen adsorption-desorption isotherm and are depicted in Table 7. Table 7 shows that HAp, HAp/Alg-11, and HAp/Alg-900 surface areas are 74.963, 162,584, and 7.161 m^2/g, respectively. In general, the surface area of HAp ranges from 70–230 m^2/g, indicating HAp nanoparticles have been formed, depending on the synthesis method. The higher surface area of HAp/Alg-11 compared to HAp and HAp/Alg-900 is associated with lower crystallinity and smaller particle size [33].

The textural properties and pore size of the HAp, HAp/Alg-11, and HAp/Alg-900 samples were determined using the adsorption-desorption of nitrogen and BJH methods, as shown in Fig. 8(a-c). The typical type IV adsorption isotherm was illustrated for all samples, and the pores ranging in size from 3 to 30 nm have mesoporous behavior reflected by the hysteresis loop with H1-type. According to the present observation, the

Table 7. Surface area and pore size comparison of the samples

Sample code	Surface areas (m^2/g)	Average pore diameter (nm)	Total pore volume (cm^3/g)
HAp	74.9630	9.3696	0.1756
HAp/Alg-11	162.5840	5.1157	0.2560
HAp/Alg-900	7.1610	5.6081	0.0100

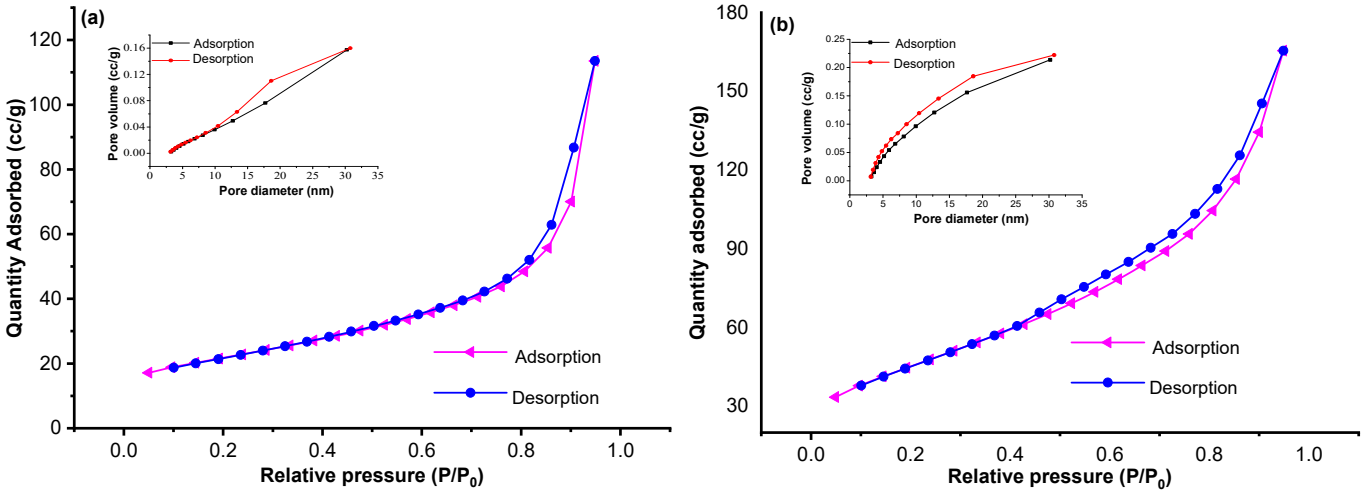

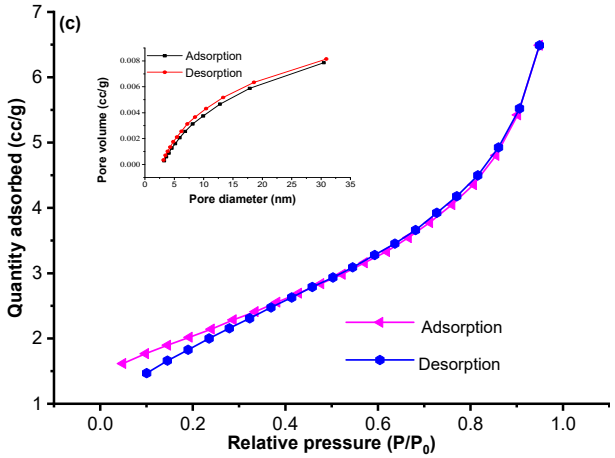

Fig 8. Adsorption-desorption of nitrogen and BJH of (a) HAp, (b) HAp/Alg-11, and (c) HAp/Alg-900

mesoporous HAp type has characteristics similar to major inorganic parts of human bone. It is becoming more and more attractive in biomedical terrain, notably for drug delivery applications.

Release Behavior of HAp and HAp/Alg Composite

The percentage of drug release was calculated to determine the possibility of HAp and HAp/Alg composites being applied as drug delivery materials. Clindamycin HCl was used as a drug model that adsorbed by HAp and HAp/Alg composite. Drug release was carried out in PBS solution with a stirring speed of 100 rpm, mimicking the condition of drugs in the human body's bloodstream. Theoretically, the release of drugs depends on the diffusion process [34].

The release profile of clindamycin by HAp, HAp/Alg-11, and HAp/Alg-900 reached 40.68, 54.82, and 37.58% in the first hour as shown in Fig. 9. Brust release at the initial time occurred because of the ion exchange between the composite and PBS solution, which led to erosion and caused the burst release of the drug [35]. Then, it increased with time to 69.65, 78.62, and 68.62% at 6 h of release in PBS, and the maximum release reached 74.48, 92.75, and 69.65% at 8 h. These results show the same trend as those reported by Tiraton et al. [18]. In the first 200 min, clindamycin HCl release has reached > 80% and is almost stable for up to 24 h. The total quantity of clindamycin delivered by microneedles 25S-75G-6C, 25S-75G-8C, and 25S-75G-10C was 90.16 ± 1.91, 92.15 ± 0.88, and 94.24 ± 2.38%, respectively, based on the actual amount of clindamycin [18].

The HAp/Alg-11 shows the maximum drug release because of the largest surface area, as shown in Table 7. The larger the surface area, the more contact with the drug, so the amount of drug absorbed is also more significant. As a result, the amount of drugs released into PBS is also increasing. Clindamycin HCl absorption is caused mainly by the electrostatic interaction between positive-charged HAp and negative-charged groups of clindamycin molecules [36]. These results confirm that alginate helps control the release of clindamycin HCl from

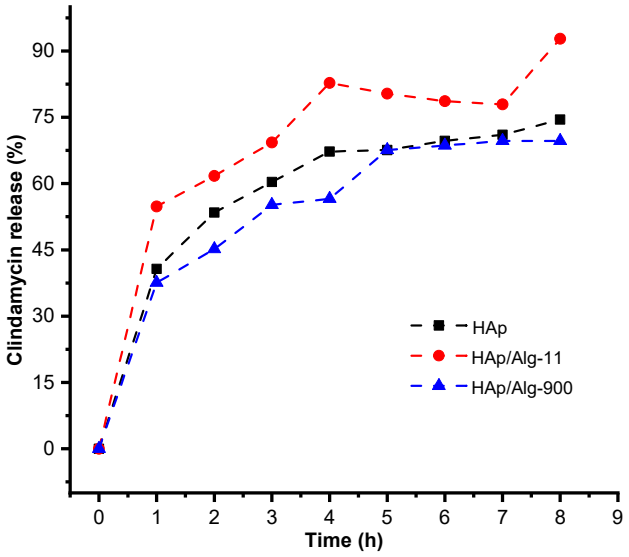

Fig 9. Clindamycin HCl release profile of HAp, HAp/Alg-11, and HAp/Alg-900

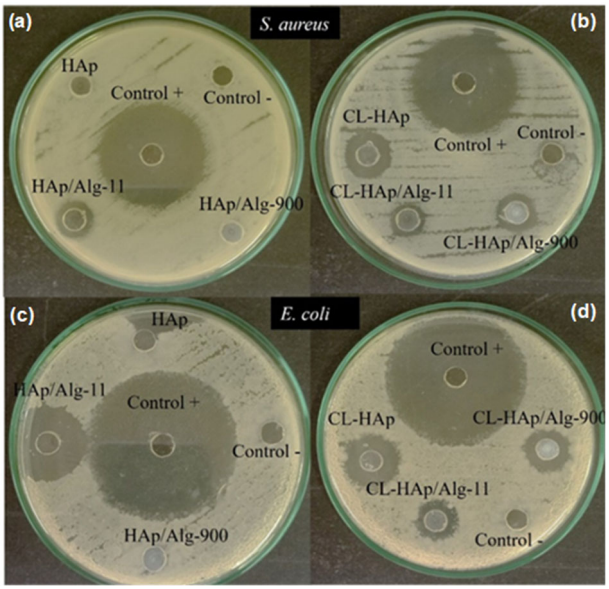

Fig 10. Antibacterial activity test of HAp, HAp/Alg-11, and HAp/Alg-900 against *S. aureus* and *E. coli* bacteria before drug loading (a & c), and after drug loading (b & d)

the material carrier to prolong the diffusion process [37].

Antibacterial Assay

The antibacterial activity test of HAp, HAp/Alg-11, and HAp/Alg-900 composites before and after loading the drug against *S. aureus* and *E. coli* bacteria is shown in Fig. 10. In Fig. 10(a, c), it can be seen that there is no zone of inhibition of HAp against *S. aureus*. However, there is a zone of inhibition against *E. coli*, although unevenly distributed. It shows that HAp has antibacterial activity, but it depends on the type of bacteria. It is consistent with what was reported by Abdulkareem et al. [13] that HAp exhibits antibacterial properties against both Gram-negative and Gram-positive bacteria. This is attributed to its capacity to enter the bacterial cell wall through electrostatic interactions with HAp, as well as the subsequent reformation of HAp within the cell. However, the effectiveness of this mechanism may vary depending on the specific characteristics of the bacterial species.

HAp/Alg-11 composite has antibacterial activity, where the inhibition zone formed is 6 mm against *S. aureus* and 18 mm against *E. coli*. In contrast, HAp/Alg-900 does not have antibacterial activity against *S. aureus* and *E. coli*, as seen from the absence of an inhibition zone formed. It is because HAp/Alg-11 contains alginate, which has antibacterial activity, while in HAp/Alg-900, the alginate has evaporated due to high heating at 900 °C. These results were compared with the positive control, namely the antibiotic clindamycin HCl, which has an inhibition zone diameter of 31 mm against *S. aureus* and 43 mm against *E. coli*. Fig. 10(b, d) shows the inhibition zone of (clindamycin HCl loaded) HAp, HAp/Alg-11, and HAp/Alg-900 or clindamycin HCl loaded composite. The diameter of the inhibition zone of these three samples tends to increase after loading the drug. It indicates that the three samples can absorb the drug to be applied as drug delivery materials.

■ CONCLUSION

The HAp/Alg composite from bamboo shells (*Sollen* spp.) had been successfully synthesized using precipitation. The results showed that the crystallinity, morphological, and chemical characteristics of the HAp depended on synthesis parameters, mostly the setting pH value and the selected sintering temperature during the synthesis process. The drug release of the sample was investigated and HAp/Alg-11 has the maximum clindamycin HCl release. Antibacterial test results showed HAp/Alg-11 has antibacterial activity against *S. aureus* and *E. coli*. HAp/Alg-11 composite has the potential to be developed as a drug carrier material.

■ ACKNOWLEDGMENTS

This work was supported by Kementerian Riset dan Teknologi/Badan Riset dan Inovasi Nasional Republik Indonesia 2022 (grant number T/17/UN.16.17/PT.01.03/PPS-PMDSU-Material Maju/2022) through the PMDSU Scholarship.

■ CONFLICT OF INTEREST

The authors declare that they have no known competing financial interests or personal relationships that could have appeared to influence the work reported in this paper.

■ AUTHOR CONTRIBUTIONS

Wulandari conducted the experiment, Wulandari and Dini Muthi'ah Islami drafted the manuscript, Novesar Jamarun, Diana Vanda Wellia, and Emriadi

wrote and revised the manuscript. All authors read and approved the final manuscript.

■ REFERENCES

[1] Lu, Y., Dong, W., Ding, J., Wang, W., and Wang, A., 2019, "Hydroxyapatite Nanomaterials: Synthesis, Properties, and Functional Applications" in *Nanomaterials from Clay Minerals: A New Approach to Green Functional Materials*, Eds. Wang, A., and Wang, W., Elsevier, Cambridge, MA, US, 485–536.

[2] Labanni, A., Zulhadjri, Z., Handayani, D., Ohya, Y., and Arief, S., 2020, Size controlled synthesis of well-distributed nano-silver on hydroxyapatite using alkanolamine compounds, *Ceram. Int.*, 46 (5), 5850–5855.

[3] Kumar, G.S., Karunakaran, G., Girija, E.K., Kolesnikov, E., Van Minh, N., Gorshenkov, M.V., and Kuznetsov, D., 2018, Size and morphology-controlled synthesis of mesoporous hydroxyapatite nanocrystals by microwave-assisted hydrothermal method, *Ceram. Int.*, 44 (10), 11257–11264.

[4] Hariani, P.L., Rachmat, A., Said, M., and Salni, S., 2021, Modification of fishbone-based hydroxyapatite with $MnFe_2O_4$ for efficient adsorption of Cd(II) and Ni(II) from aqueous solution, *Indones. J. Chem.*, 21 (6), 1471–1483.

[5] Islami, D.M., Wulandari, W., Jamarun, N., Syukri, S., and Sisca, V., 2023, *In-situ* hydrothermal method for graphene oxide/hydroxyapatite synthesis from scallop shells, *Rasayan J. Chem.*, 16 (1), 456–462.

[6] Haider, A., Haider, S., Han, S.S., and Kang, I.K., 2017, Recent advances in the synthesis, functionalization and biomedical applications of hydroxyapatite: A review, *RSC Adv.*, 7 (13), 7442–7458.

[7] Ali, A., Hasan, A., and Negi, Y.S., 2022, Effect of carbon based fillers on xylan/chitosan/nano-HAp composite matrix for bone tissue engineering application, *Int. J. Biol. Macromol.*, 197, 1–11.

[8] Noviyanti, A.R., Akbar, N., Deawati, Y., Ernawati, E.E., Malik, Y.T., Fauzia, R.P., and Risdiana, R., 2020, A novel hydrothermal synthesis of nanohydroxyapatite from eggshell-calcium-oxide precursors, *Heliyon*, 6 (4), e03655.

[9] Wulandari, W., Islami, D.M., Wellia, D.V., Emriadi, E., Sisca, V., and Jamarun, N., 2023, The effect of alginate concentration on crystallinity, morphology, and thermal stability properties of hydroxyapatite/alginate composite, *Polymers*, 15 (3), 614.

[10] Lazić, V., Smičiklas, I., Marković, J., Lončarević, D., Dostanić, J., Ahrenkiel, S.P., and Nedeljković, J.M., 2018, Antibacterial ability of supported silver nanoparticles by functionalized hydroxyapatite with 5-aminosalicylic acid, *Vacuum*, 148, 62–68.

[11] Wan, F., Ping, H., Wang, W., Zou, Z., Xie, H., Su, B.L., Liu, D., and Fu, Z., 2021, Hydroxyapatite-reinforced alginate fibers with bioinspired dually aligned architectures, *Carbohydr. Polym.*, 267, 118167.

[12] Madhumathi, K., Binulal, N.S., Nagahama, H., Tamura, H., Shalumon, K.T., Selvamurugan, N., Nair, S.V., and Jayakumar, R., 2009, Preparation and characterization of novel β-chitin–hydroxyapatite composite membranes for tissue engineering applications, *Int. J. Biol. Macromol.*, 44 (1), 1–5.

[13] Abdulkareem, M.H., Abdalsalam, A.H., and Bohan, A.J., 2019, Influence of chitosan on the antibacterial activity of composite coating (PEEK/HAp) fabricated by electrophoretic deposition, *Prog. Org. Coat.*, 130, 251–259.

[14] Apriliyanto, Y.B., Sugiarti, S., and Sukaryo, S.G., 2020, Enhancing thermal and mechanical properties of UHMWPE/HA composite as tibial tray, *Indones. J. Chem.*, 20 (3), 597–607.

[15] Sanchez, A.G., Prokhorov, E., Luna-Barcenas, G., Hernández-Vargas, J., Román-Doval, R., Mendoza, S., and Rojas-Chávez, H., 2021, Chitosan-hydroxyapatite-MWCNTs nanocomposite patch for bone tissue engineering applications, *Mater. Today Commun.*, 28, 102615.

[16] Adhikari, J., Perwez, M.S., Das, A., and Saha, P., 2021, Development of hydroxyapatite reinforced alginate–chitosan based printable biomaterial-ink, *Nano-Struct. Nano-Objects*, 25, 100630.

[17] Rahyussalim, A.J., Aprilya, D., Handidwiono, R., Whulanza, Y., Ramahdita, G., and Kurniawati, T., 2022, The use of 3D polylactic acid scaffolds with

hydroxyapatite/alginate composite injection and mesenchymal stem cells as laminoplasty spacers in rabbits, *Polymers*, 14 (16), 3292.

[18] Tiraton, T., Suwantong, O., Chuysinuan, P., Ekabutr, P., Niamlang, P., Khampieng, T., and Supaphol, P., 2022, Biodegradable microneedle fabricated from sodium alginate-gelatin for transdermal delivery of clindamycin, *Mater. Today Commun.*, 32, 104158.

[19] Nigam, A., and Pawar, S.J., 2020, Structural, magnetic, and antimicrobial properties of zinc doped magnesium ferrite for drug delivery applications, *Ceram. Int.*, 46 (4), 4058–4064.

[20] Yuvaraj, S., Muthukumarasamy, N., Flores, M., Rajesh, G., Paraskevopoulos, K.M., Pouroutzidou, G.K., Theodorou, G.S., Ioannidou, K., Lusvarghi, L., Velauthapillai, D., and Yoganand, C.P., 2021, Incorporation of nanosized carbon over hydroxyapatite (HAp) surface using DC glow discharge plasma for biomedical application, *Vacuum*, 190, 110300.

[21] Sun, Y., Yang, H., and Tao, D., 2011, Microemulsion process synthesis of lanthanide-doped hydroxyapatite nanoparticles under hydrothermal treatment, *Ceram. Int.*, 37 (7), 2917–2920.

[22] Zheng, Y., Wang, L., Bai, X., Xiao, Y., and Che, J., 2022, Bio-inspired composite by hydroxyapatite mineralization on (bis)phosphonate-modified cellulose-alginate scaffold for bone tissue engineering, *Colloids Surf., A*, 635, 127958.

[23] Prekajski Đorđević, M., Maletaškić, J., Stanković, N., Babić, B., Yoshida, K., Yano, T., and Matović, B., 2018, *In-situ* immobilization of Sr radioactive isotope using nanocrystalline hydroxyapatite, *Ceram. Int.*, 44 (2), 1771–1777.

[24] Sirajudheen, P., Karthikeyan, P., Vigneshwaran, S., Basheer, M.C., and Meenakshi, S., 2021, Complex interior and surface modified alginate reinforced reduced graphene oxide-hydroxyapatite hybrids: Removal of toxic azo dyes from the aqueous solution, *Int. J. Biol. Macromol.*, 175, 361–371.

[25] Jariya, S.A.I., Padmanabhan, V.P., Kulandaivelu, R., Prakash, N., Mohammad, F., Al-Lohedan, H.A., Paiman, S., Schirhagl, R., Hossain, M.A.M., and Sagadevan, S., 2021, Drug delivery and antimicrobial studies of chitosan-alginate based hydroxyapatite bioscaffolds formed by the Casein micelle assisted synthesis, *Mater. Chem. Phys.*, 272, 125019.

[26] Laput, O.A., Zuza, D.A., Vasenina, I.V., Savkin, K.P., and Kurzina, I.A., 2020, Effect of silver ion implantation on surface physicochemical properties of composite materials based on polylactic acid and hydroxyapatite, *Vacuum*, 175, 109251.

[27] Bera, M., Gupta, P., and Maji, P.K., 2018, Facile one-pot synthesis of graphene oxide by sonication assisted mechanochemical approach and its surface chemistry, *J. Nanosci. Nanotechnol.*, 18 (2*)*, 902–912.

[28] Victoria, E.C., and Robinson M, C., 2019, Comparative studies on synthesis and sintering studies of biologically derived hydroxyapatite from *Capria hircus* (Goat) and *Bos primigenius* (Bovine), *Vacuum*, 160, 378–383.

[29] Palanivelu, R., Mary Saral, A., and Ruban Kumar, A., 2014, Nanocrystalline hydroxyapatite prepared under various pH conditions, *Spectrochim. Acta, Part A*, 131, 37–41.

[30] Rodríguez-Lugo, V., Karthik, T.V.K., Mendoza-Anaya, D., Rubio-Rosas, E., Villaseñor Cerón, L.S., Reyes-Valderrama, M.I., and Salinas-Rodríguez, E., 2018, Wet chemical synthesis of nanocrystalline hydroxyapatite flakes: Effect of pH and sintering temperature on structural and morphological properties, *R. Soc. Open Sci.*, 5 (8), 180962.

[31] Jarudilokkul, S., Tanthapanichakoon, W., and Boonamnuayvittaya, V., 2007, Synthesis of hydroxyapatite nanoparticles using an emulsion liquid membrane system, *Colloids Surf., A*, 296 (1), 149–153.

[32] Chen, B.H., Chen, K.I., Ho, M.L., Chen, H.N., Chen, W.C., and Wang, C.K., 2009, Synthesis of calcium phosphates and porous hydroxyapatite beads prepared by emulsion method, *Mater. Chem. Phys.*, 113 (1), 365–371.

[33] Lakrat, M., Jodati, H., Mejdoubi, E.M., and Evis, Z., 2023, Synthesis and characterization of pure and Mg, Cu, Ag, and Sr doped calcium-deficient hydroxyapatite from brushite as precursor using

the dissolution-precipitation method, *Powder Technol.*, 413, 118026.

[34] Czarnecka, B., and Nicholson, J.W., 2013, The use of alginate impression material for the controlled release of sodium fusidate, *Dent. Forum*, XLI (1), 11–14.

[35] Hasnain, M.S., Nayak, A.K., Singh, M., Tabish, M., Ansari, M.T., and Ara, T.J., 2016, Alginate-based bipolymeric-nanobioceramic composite matrices for sustained drug release, *Int. J. Biol. Macromol.*, 83, 71–77.

[36] Pradid, J., Keawwatana, W., Boonyang, U., and Tangbunsuk, S., 2017, Biological properties and enzymatic degradation studies of clindamycin-loaded PLA/HAp microspheres prepared from crocodile bones, *Polym. Bull.*, 74 (12), 5181–5194.

[37] Seidenstuecker, M., Ruehe, J., Suedkamp, N.P., Serr, A., Wittmer, A., Bohner, M., Bernstein, A., and Mayr, H.O., 2017, Composite material consisting of microporous β-TCP ceramic and alginate for delayed release of antibiotics, *Acta Biomater.*, 51, 433–446.